

Two-dimensional computational simulation of eccentric annular cementing displacements

S. Pelipenko

Etudes et Productions Schlumberger, 1, rue Becquerel, 92140 Clamart - France.

I.A. Frigaard

*Department of Mathematics and Department of Mechanical Engineering,
University of British Columbia, 2324 Main Mall, Vancouver, BC, Canada, V6T
1Z4.*

Abstract

We consider a two-dimensional Hele-Shaw type model for displacement flows occurring in the primary cementing of an oil well. The fluids are visco-plastic and may get stuck in the annulus if a critical pressure gradient is not exceeded. The model consists of solving a nonlinear elliptic variational inequality equation for the stream function, coupled to an equation for interface advection, or alternatively a concentration equation for the mass fraction of each fluid. The key difficulty is to accurately compute yielded and unyielded zones of the wellbore fluids, which we accomplish by use of an augmented Lagrangian method to solve the stream function equation. We validate the accuracy of our method against analytical solutions for stable steady state displacements. We study the convergence of the interface to the steady state, showing that the apparent meta-stability is illusory. We then explore the effects of increasing eccentricity, showing that although the interface may remain stable it becomes unsteady. Initially fully mobile flows are found, but as the eccentricity increases further the narrow side fluids fail to move in the far-field. The narrow side interface can progress slowly through the static fluids by a burrowing motion, but for still larger eccentricities even the interface becomes static and a narrow-side mud channel forms.

Key words: Hele-Shaw cell, displacement flows, variational methods, augmented Lagrangian, visco-plastic fluid flow.

1 Introduction

In construction of oil and gas wells it is necessary to cement a series of steel casings into the well, as the length of the well increases. This is done both to

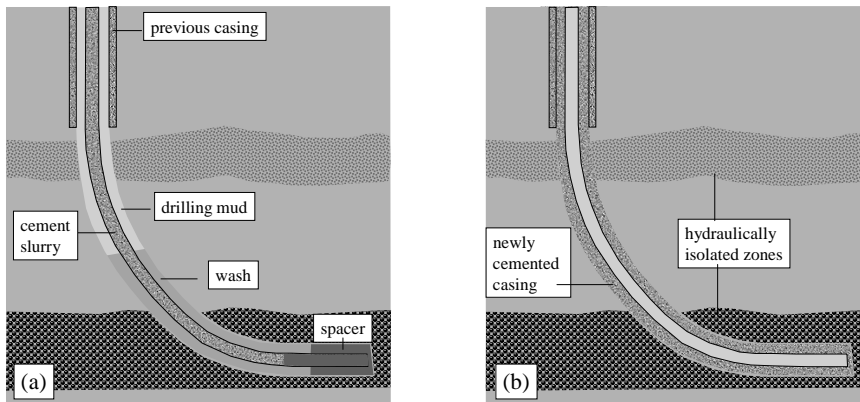


Fig. 1. Schematic of the primary cementing process: (a) during and (b) after cementing a new casing.

structurally strengthen the sides of the wellbore and to provide zonal isolation along the length of the well. Zonal isolation means achieving an hydraulic seal on the outside of the steel casing, between casing and rock formation, along the length of the well. The process by which this is commonly achieved is called primary cementing, (see e.g. [1,2]).

The primary cementing process proceeds as follows, [1,3]. After a new section of the well is drilled, the drill pipe is removed from the wellbore, leaving the drilling mud behind. A section of the steel casing is then inserted into the hole, leaving a small annular gap (~ 2 cm) between the outside of the casing and the rock, i.e. forming an annulus. Centralizers are fitted to the outside of the casing to prevent the steel tubing from slumping to the lower side of the wellbore. Fitting centralizers can slow insertion of the casing into the well or cause it to stick. Consequently there are often either not enough centralizers or the centralizers are poorly positioned. It is therefore extremely common that the annulus is eccentric. After the casing is in place, a sequence of fluids is pumped down the inside of the casing, reaching the bottom of the well and returning upwards through the annular gap, each successive fluid displacing the previous fluid. Typically, a wash or spacer fluid is pumped first, followed by one or more cement slurries. Drilling mud follows the final cement slurry pumped and circulation is stopped with a few meters of cement left at the bottom inside the casing. The cement is then allowed to set, taking a number of hours. Finally, drilling resumes through the residual few meters of cement inside the casing and further into the underlying rock, see Fig. 1.

A successful cement job results in removal of mud and spacer fluid from the annulus by the cement slurry. Unfortunately, mud is sometimes left behind in parts of the annulus. As the cement sets water is removed from it, producing a porous channel along which reservoir fluids can migrate upwards. Various serious problems can arise from such uncontrolled flows. From the

financial perspective, an hydraulic connection between different fluid bearing zones tends to equilibrate pressures. Typically the reservoir is in the lower, higher pressure zone and the reduction in reservoir pressure can result in a significant loss in productivity, [4]. Secondly, gas or oil may flow to surface causing a blowout, with consequent environmental damage and possible loss of life. Reservoir fluids may migrate into a subsurface aquifer causing contamination of drinking water, or affecting near-wellbore ecology. Finally, even when these flows are contained within the annulus, the fact of having pressure at surface prevents a well from being permanently abandoned. These wells become permanently shut-in and remain an environmental risk. A widely cited industry figure, e.g. [5], is that 15% of primary cementing jobs carried out in the US fail and that about 1/3 of these failures are due to gas or fluid migration. This problem exists worldwide, (e.g. about 9000 wells are suspended or temporarily abandoned in the U.S. Gulf Coast region, in Western Canada around 34,000 wells are shut-in and suspended, [6]). There can also be wide local variations in this problem. For example, field survey results are reported in [7], from Tangleflags, Wildmere and Abbey, (3 areas in Eastern Alberta). Over a number of years, 0 – 12% (Tangleflags), 0 – 15% (Wildmere), and 80% (Abbey) of wells are reported as leaking in these regions. This industrial background provides the motivation for our study of cementing displacement flows.

To facilitate mud removal it is possible to modify, (i.e. design), the rheologies and densities of the spacer fluid and cement slurry and to choose the pumping rate, all within the constraints of maintaining well security. In general the fluids involved are inelastic shear-thinning fluids with a yield stress. In the industry, these are modelled as incompressible Herschel-Bulkley fluids, i.e. the constitutive relation between shear stress, τ , and rate of strain, $\dot{\gamma}$, is given by:

$$\tau = \tau_Y + \kappa \dot{\gamma}^n, \quad (1)$$

where τ_Y is the yield stress, κ is the consistency and n is power law index of the fluid. Thus, we are led to the design problem of how best to displace one non-Newtonian fluid with another, along an eccentric annulus. For the purpose of this paper, we consider only flows which are laminar. This occurs frequently in wells where the pumping rates are limited, e.g. due to the danger of exceeding the formation fracture pressure in turbulent regime.

The majority of the technical literature on modelling laminar cementing displacement has followed one of two approaches. First, many authors have used what might be described as an hydraulic or mechanical approach. Such approaches consider the flow of a single fluid along a duct and make predictions based on comparisons of the hydraulic characteristics of these flows for the different fluids being pumped, e.g. is there a flow, comparing frictional pressures and flow rates. At a very early stage, [8], the possibility of mud being

stuck on the narrow side of the annulus was recognised using these methods. Extensions of this approach have led to whole systems of design rules for a successful cementing job, [9–12]. These rule sets are mostly applicable to near-vertical wells and share certain common features. For example, they state that the flow should be sufficiently high to avoid a static mud channel on the narrow side of the annulus and that there should be a positive gradient of both the rheological parameters and densities, i.e. so that each fluid is heavier than the one it displaces and generates higher frictional pressure. While such systems can be applied to good effect, [13,14], they tend to be conservative and experience problems with predicting flows in highly-deviated sections of the well.

The second approach has been to model the displacement flow fully in 3-D. Researchers have followed this approach, both using commercially available CFD software, [15,16], and by developing dedicated algorithms, e.g. [17]. A drawback of any 3D approach is the difficulty of modelling displacement flows over the length-scale of the wellbore. The difficulty here is three-fold. First, for accuracy on the annular gap scale ($\sim 0.01\text{m}$), a vast number of mesh points are needed to represent both the annular circumference scale ($\sim 0.5\text{m}$), and axial length-scale ($\sim 100\text{m}$). Second, it is known that significant secondary flows occur near the interface in such flows, [17–19]. The magnitude of azimuthal velocities can be of a similar order to the axial velocities close to the interface. Thus, CFL-type restrictions on time-stepping can be severe and at the same time it is necessary to integrate over long timescale to simulate a complete job. Thus in general, such approaches have focused on a small section of the annulus. A third problem concerns the use of currently available CFD tools for correctly modelling both non-Newtonian behaviour and interface motion. For example, most currently available CFD software codes do not model real yield stress behaviour, but instead use some form of regularised viscosity model at low shear. Whilst this approach has some justification in a steady flow of a single fluid, for unsteady flows of multiple fluids, particularly those occurring over long timescales, it becomes questionable.

The purpose of this paper is to show how a two-dimensional computer simulation of the primary cementing process may be carried out, that allows one to accurately identify those features of the process that are useful for design. To this end we follow the modelling approach in [18,19], which is derived from an earlier approach in [20,21]. Whereas the model derived in [18] relates to the entire wellbore, we focus here on a uniform section of eccentric annulus. This may be either interpreted as modelling a short section of the wellbore along which the geometry is constant, (e.g. a length of a few meters would be realistic), or may be interpreted as a suitable model for a laboratory-scale experiment. Although a slight simplification, the computational method that we use is equally applicable to modelling the entire well. The general idea of the model derived in [18] is to assume homogeneity of the fluid across the annular

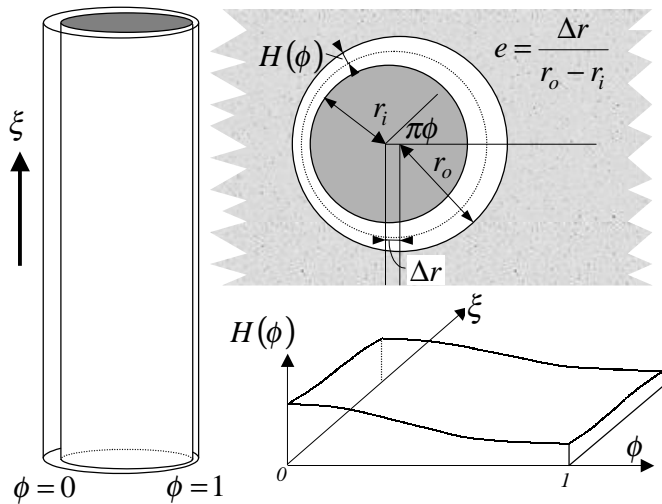


Fig. 2. Geometry of the narrow eccentric annulus, mapped to the Hele-Shaw cell geometry.

gap, average in the radial direction across the annular gap and employ various scaling arguments to reduce the three-dimensional Navier-Stokes equations to a two-dimensional Hele-Shaw type model, in axial and azimuthal directions, see Fig. 2. This approach avoids the difficulties of discretising the annulus on the smallest (annular gap) scale. The length of the well is still long with respect to the azimuthal scale and the inherent problems of integrating over a long time do remain, but these problems are much reduced in comparison to a fully 3D approach. The only other drawback of the Hele-Shaw approach is that we in effect ignore the possibility that a layer of mud can remain stuck to the casing or the formation. These possibilities can be studied by considering near-axial displacement flows in a long duct. Such investigations are ongoing, [23–26].

2 Modelling cementing displacements

We outline a simplified version of the model in [18,19], which we shall study in this paper. The simplification that we make is that the annulus is locally uniform in the axial direction, i.e. over a length-scale that is long in comparison to the azimuthal scale. This is easily justified for the slowly varying geometries of typical wells. We address the displacement dynamics in one such section.

Consider therefore a uniform section of annulus with axis at fixed angle of inclination, β , to the vertical. The model in [18,19] consists of averaging across the narrow annular gap to eliminate radial variations, thus effectively *unwrapping* the annulus into a Hele-Shaw cell, see Fig. 2. Dimensionless spatial coordinates are $(\phi, \xi) \in (0, 1) \times (0, Z)$. Here ϕ is the azimuthal coordinate with

$\phi = 0$ denoting the wide side of the annulus and $\phi = 1$ the narrow (lower) side. The flow is assumed symmetric about $\phi = 0$, and thus only half the annulus is considered. The ξ coordinate measures axial depth upwards along the annulus, see Fig. 2. The annulus is initially full of fluid 1, which is displaced by fluid 2. The scaled leading order model derived in [18] consists of the following field equations.

$$\frac{\partial}{\partial t} [H\bar{c}] + \frac{\partial}{\partial \phi} [H\bar{v} \bar{c}] + \frac{\partial}{\partial \xi} [H\bar{w} \bar{c}] = 0, \quad (2)$$

$$\nabla \cdot \mathbf{S} = -f, \quad (3)$$

where \bar{c} denotes the concentration of fluid 1, $H(\phi)$ is the annular half-gap width:

$$H(\phi) = 1 + e \cos \pi \phi, \quad (4)$$

where $e \in [0, 1)$ is the annulus eccentricity; $e = 0$ corresponds to a concentric annulus, $e = 1$ implies contact between casing and outer wall, on the narrow side of the annulus. The averaged velocity components in (ϕ, ξ) -directions are (\bar{v}, \bar{w}) . The fluids are considered incompressible and (\bar{v}, \bar{w}) are defined via a stream-function Ψ :

$$\frac{\partial \Psi}{\partial \phi} = H\bar{w}, \quad \frac{\partial \Psi}{\partial \xi} = -H\bar{v}. \quad (5)$$

In (3), the vector field \mathbf{S} is defined by

$$\mathbf{S} = \left[\frac{\chi(|\nabla \Psi|) + \tau_Y/H}{|\nabla \Psi|} \right] \nabla \Psi \iff |S| > \frac{\tau_Y}{H}, \quad (6)$$

$$|\nabla \Psi| = 0 \iff |S| \leq \frac{\tau_Y}{H}. \quad (7)$$

where $(\chi + \tau_Y/H)$ corresponds dimensionlessly, to the absolute value of the modified pressure gradient required to push an areal flow rate $|\nabla \Psi|$ through a plane channel of half-width H . The function χ is defined implicitly from the relation:

$$|\nabla \Psi| = \begin{cases} 0 & \chi \leq 0, \\ \frac{H^{m+2}}{\kappa^m(m+2)} \frac{\chi^{m+1}}{(\chi + \tau_Y/H)^2} \left[\chi + \frac{(m+2)\tau_Y}{(m+1)H} \right] & \chi > 0. \end{cases} \quad (8)$$

The underlying fluid model used is the Herschel-Bulkley model; $m = 1/n$ is the inverse power index, τ_Y is the yield stress and κ is the consistency. Thus,

$\chi = \chi(|\nabla\Psi|; H, \tau_Y, \kappa, m)$ although for brevity we shall write $\chi(|\nabla\Psi|)$, and later we will write χ_k to denote the function $\chi(|\nabla\Psi|; H, \tau_{k,Y}, \kappa_k, m_k)$ where $(\tau_{k,Y}, \kappa_k, m_k)$ are the rheological properties of fluid k . All buoyancy terms have been collected on the right hand side of (3) in the term f :

$$f = \nabla \cdot \left(\frac{\rho(\bar{c}) \cos \beta}{St^*}, \frac{\rho(\bar{c}) \sin \beta \sin \pi \phi}{St^*} \right) = \nabla \cdot \tilde{\mathbf{f}}, \quad (9)$$

where St^* is the global Stokes number for the flow, (typically $St^* < 1$). The derivation of this model is explained in detail in [18].

Boundary conditions for (2) are symmetry of concentration at $\phi = 0, 1$, and specification of any inflowing fluid concentrations at the ends, $\xi = 0, Z$, i.e. $\bar{c} = 0$ or $\bar{c} = 1$, accordingly. For the stream function equation (3), boundary conditions are

$$\Psi(0, \xi, t) = 0, \quad \Psi(1, \xi, t) = 1, \quad (10)$$

$$\frac{\partial \Psi}{\partial \xi}(\phi, Z, t) = 0, \quad \frac{\partial \Psi}{\partial \xi}(\phi, 0, t) = 0. \quad (11)$$

The above model is that which we shall use for our computations in this paper, but some variants should also be noted.

2.1 Pressure formulation

Typically, a Hele-Shaw model is formulated in terms of the pressure field and this is also possible here. The two components of $\mathbf{S} = (S_\phi, S_\xi)$ have the alternative interpretation as:

$$S_\phi = -\frac{\partial p}{\partial \xi} - \frac{\rho(\bar{c}) \cos \beta}{St^*}, \quad S_\xi = \frac{\partial p}{\partial \phi} - \frac{\rho(\bar{c}) \sin \beta \sin \pi \phi}{St^*}, \quad (12)$$

from which it is possible to eliminate the stream function and derive a pressure equation in place of (3). However, the pressure will be indeterminate in regions where $|S| \leq \tau_Y/H$, and for this reason the stream-function formulation is preferable. We note that this is also the case in porous media flows with a limiting pressure gradient, which are mathematically similar, see e.g. [30,31].

2.2 Interface tracking

The formulation with (2) requires one to interpret the interface as a level line of the concentration field, e.g. $\bar{c}(\phi, \xi, t) = 0.5$, and also to specify closure laws for the mixture fluid properties, i.e. as functions of \bar{c} . In [19] we have also derived an alternative formulation that tracks the interface using a kinematic equation, as opposed to solving (2) for the concentration. The domain is divided into two fluid domains: Ω_1 for the displacing (lower) fluid 1, and Ω_2 for the displaced (upper) fluid 2, in each of which (3) is replaced by:

$$\nabla \cdot \mathbf{S}_1 = 0, \quad (\phi, \xi) \in \Omega_1, \quad (13)$$

$$\nabla \cdot \mathbf{S}_2 = 0, \quad (\phi, \xi) \in \Omega_2, \quad (14)$$

with \mathbf{S}_1 and \mathbf{S}_2 defined as in (6-7), with properties $\rho_1, \tau_{1,Y}, \kappa_1, m_1$ in fluid 1 and $\rho_2, \tau_{2,Y}, \kappa_2, m_2$ in fluid 2. The interface is denoted by $\xi = h(\phi, t)$, and satisfies the kinematic condition:

$$\frac{\partial h}{\partial t} + \bar{v} \frac{\partial h}{\partial \phi} = \bar{w}. \quad (15)$$

The leading order continuity conditions at the interface are that the stream function Ψ and the pressure p are continuous across the interface. Assuming sufficient regularity of the interface, the former condition assures that the normal velocity, (i.e. the derivative of Ψ along the interface), is well defined at the interface. Differentiating the pressure along the interface, we find:

$$\left[\left(S_{k,\xi} - S_{k,\phi} \frac{\partial h}{\partial \phi} \right) + \left(\frac{\rho_k \sin \beta \sin \pi \phi}{St^*} - \frac{\rho_k \cos \beta}{St^*} \frac{\partial h}{\partial \phi} \right) \right]_1^2 = 0. \quad (16)$$

In the case that the fluid is yielded at the interface, (16) defines the jump in normal derivative of Ψ across the interface.

3 Computational solution

The field equations (2) & (3) are in convenient form for creating a numerical simulation of a displacement flow. Equation (3) allows us to calculate the stream function, and hence velocity field, given a specific concentration field at time t^l . Equation (2) specifies how to advance this concentration to time t^{l+1} , using the computed velocity field. Equation (2) is a standard conservation equation, with conserved quantity $H\bar{c}$. A wide range of numerical algorithms exist for its solution. Thus, here we focus on solution of (3). Equation (3) is a

non-linear elliptic equation for Ψ and in its classical formulation is not well-defined at $|\nabla\Psi| = 0$. A mathematically consistent formulation of the boundary value problem associated with (3) is as an elliptic variational inequality. This is the approach adopted in [19], where it is proven that there exists a unique weak solution.

To date, two approaches have been used to solve (3). First in [19], using the interface-tracking formulation described above, analytical solutions were derived for steady state displacements, i.e. travelling wave solutions that advance at the mean (pumping) fluid velocity. The second approach, described in [18], assumes that gradients in the axial direction are much less than those in the azimuthal direction. A regular perturbation expansion, with small parameter $\varepsilon = 1/Z \ll 1$, is used for all dependent variables. Upon substituting $\Psi \sim \Psi_0 + \varepsilon\Psi_1 + \dots$, into (3), the field equation reduces to a series of one-dimensional boundary value problems that are solved on individual axial depth slices, i.e. at fixed values of ξ . This leads to a very rapid and robust numerical solution for Ψ . Additionally, the computational time scales linearly with the number of grid-points used to discretise the annulus. Whilst adequate for many applications one key drawback remains, namely that the two-dimensional field equation (3) derived in the model is not actually solved, only its perturbation approximation. In this paper we adopt a third approach, which solves (3) fully.

3.1 Augmented Lagrangian algorithm for Ψ

The method we employ in this paper uses an augmented Lagrangian algorithm to solve the fully 2D problem for Ψ . The key advantage of this method for visco-plastic fluid flows is the direct computation of unyielded regions in the flow, i.e. where $|\nabla\Psi| = 0$, with no need for any form of viscosity regularisation. The method is developed for classes of similar problems in [27,28], and an example of its application to the axial flow of a single Bingham fluid in an annular duct is given in [29]. Consequently, we give only a brief outline of the algorithm here.

Using methods as in [19], the BVP for Ψ can be expressed as the following minimisation problem:

$$\min_{v \in \mathbb{V}_0(\Omega)} \{J(v)\}, \quad (17)$$

where $\Omega = (0, 1) \times (0, Z)$ and $J(v) = F(\nabla v)$, with

$$F(\mathbf{q}) = F_0(\mathbf{q}) + F_1(\mathbf{q}), \quad \mathbf{q} \in X, \quad \text{where} \quad (18)$$

$$F_0(\mathbf{q}) = \int_{\Omega} \left(\frac{1}{2} \int_0^{|\nabla\Psi^* + \mathbf{q}|^2} \frac{\chi(s^{1/2})}{s^{1/2}} ds + \mathbf{q} \cdot \tilde{\mathbf{f}} \right) d\Omega, \quad \mathbf{q} \in X, \quad (19)$$

$$F_1(\mathbf{q}) = \int_{\Omega} \frac{\tau_Y}{H} |\nabla\Psi^* + \mathbf{q}| d\Omega, \quad \mathbf{q} \in X. \quad (20)$$

Remark 3.1: We have homogenized the essential boundary conditions along $\phi = 0$ and $\phi = 1$, by setting

$$\Psi = \Psi^* + \Phi, \quad \Psi^* \in \bar{V}(\Omega), \quad \Phi \in \bar{V}_0(\Omega) \quad (21)$$

with suitably constructed Ψ^* ; here we shall use

$$\Psi^* = \phi + \frac{e}{\pi} \sin \pi\phi. \quad (22)$$

Remark 3.2: In the above, in the continuous setting we take

$$V_0(\Omega) = \{v \in C^\infty(\Omega) : v(0, \xi) = 0, v(1, \xi) = 0\},$$

$$V(\Omega) = \{v \in C^\infty(\Omega) : v(0, \xi) = 0, v(1, \xi) = 1\},$$

and the test spaces $\bar{V}_0(\Omega)$ and $\bar{V}(\Omega)$ are the closures of $V_0(\Omega)$ and $V(\Omega)$, respectively, with respect to the $W^{1,1+1/m}(\Omega)$ norm, (here m is the maximal value of inverse power law index in the domain). The space $X = L^{1+1/m}(\Omega) \times L^{1+1/m}(\Omega)$. In [19] it is shown that $F_0(q)$ is strictly convex and differentiable and $F_1(q)$ is convex. Results from [27,28] are then applied to show that this minimisation problem has a unique solution $\Phi \in \bar{V}_0(\Omega)$, and hence there exists a unique $\Psi \in \bar{V}(\Omega)$.

Remark 3.3: Application of the augmented Lagrangian algorithm, as we do here, and use of the associated convergence results in [27,28] requires the solution space to be a Hilbert space, but $\bar{V}_0(\Omega)$ will only be a Hilbert space for $m \leq 1$. It is more common however for the fluids used in primary cementing to be shear-thinning, that is with $m = 1/n > 1$. Nevertheless, once the variational problem has been approximated by a finite-dimensional numerical method, (e.g. by finite element or finite volume method), the approximate solution space V_h , (with h denoting a mesh scale), is finite dimensional and thus is a Hilbert space. Thus, although the technical difficulty remains in the limit that $h \rightarrow 0$, in practice one computes with a small finite h . For each such h we may assume that our (finite dimensional) solution space is $\bar{V}_0(\Omega) \subset H^1(\Omega)$, and similarly we may take $X = L^2(\Omega) \times L^2(\Omega)$. For the sequel, where we consider only the finite dimensional approximation, ($\Phi = \Phi_h$, etc.), we therefore straightforwardly apply the results in [27,28] to the iterative solution

of our approximate problem. For brevity, omit all h subscripts in our variables, but it is understood that we consider only the finite dimensional setting.

3.1.1 Outline of algorithm (finite dimensional setting)

For a given constant $r > 0$ the augmented Lagrangian functional \mathbf{L}_r associated with $J(v)$ is defined by

$$\mathbf{L}_r(v, \mathbf{q}, \boldsymbol{\mu}) = F(\mathbf{q}) + \int_{\Omega} \boldsymbol{\mu} \cdot (\nabla v - \mathbf{q}) \, d\Omega + \frac{r}{2} \int_{\Omega} |\nabla v - \mathbf{q}|^2 \, d\Omega, \quad (23)$$

and we define the associated Lagrangian functional, $\mathbf{L}(v, \mathbf{q}, \boldsymbol{\mu})$, as above with $r = 0$. Following [27,28], $\{\Phi, \mathbf{p}, \boldsymbol{\lambda}\}$ is a saddle point of \mathbf{L} if and only if it is a saddle point of \mathbf{L}_r , $\forall r > 0$. Moreover such Φ is also the solution of (17) and $\mathbf{p} = \nabla \Phi$. Thus, finding the solution (17) is accomplished by finding a saddle point of \mathbf{L}_r . We do this by an iterative algorithm of Uzawa type, starting at given $\mathbf{p}^0, \boldsymbol{\lambda}^1 \in X$. Each step of the algorithm consists of finding $\Phi^n, \mathbf{p}^n, \boldsymbol{\lambda}^{n+1}$ by solving sequentially:

$$\int_{\Omega} \boldsymbol{\lambda}^n \cdot \nabla(v - \Phi^n) + (r\nabla\Phi^n - \mathbf{p}^{n-1}) \cdot \nabla(v - \Phi^n) \, d\Omega \geq 0, \quad (24)$$

$$\forall v \in \bar{V}_0, \Phi^n \in \bar{V}_0,$$

$$F(\mathbf{q}) - F(\mathbf{p}^n) - \int_{\Omega} \boldsymbol{\lambda}^n \cdot (\mathbf{q} - \mathbf{p}^n) + r(\mathbf{p}^n - \nabla\Phi^n) \cdot (\mathbf{q} - \mathbf{p}^n) \, d\Omega \geq 0, \quad (25)$$

$$\forall \mathbf{q} \in X, \mathbf{p}^n \in X.$$

$$\boldsymbol{\lambda}^{n+1} = \boldsymbol{\lambda}^n + \rho_n(\nabla\Phi^n - \mathbf{p}^n), \quad \rho_n > 0. \quad (26)$$

Following [28] we have $\Phi^n \rightarrow \Phi$ strongly in \bar{V}_0 . Also, $\mathbf{p}^n \rightarrow \mathbf{p}$ strongly in X and $\boldsymbol{\lambda}^{n+1} - \boldsymbol{\lambda}^n \rightarrow 0$ strongly in X , with $\boldsymbol{\lambda}^n$ bounded in X . The condition for convergence of the above algorithm is

$$0 < \rho_n = \rho < \frac{1 + \sqrt{5}}{2} r. \quad (27)$$

Equation (24) corresponds to minimizing $\mathbf{L}_r(v, \mathbf{p}^{n-1}, \boldsymbol{\lambda}^n)$ with respect to v to get Φ^n . This is formally equivalent to solving the following Poisson equation

$$r\nabla^2\Phi^n = r\nabla \cdot \mathbf{p}^n - \nabla \cdot \boldsymbol{\lambda}^n, \quad (28)$$

with the right hand side known at each iteration. This is obviously straightforward. The second step, solving (25), corresponds to minimizing $\mathbf{L}_r(\Phi^n, \mathbf{q}, \boldsymbol{\lambda}^n)$ with respect to \mathbf{q} , in order to obtain \mathbf{p}^n . Although the algorithm (24)-(26) is

quite general, for visco-plastic flows such as our problem, the second step is the critical one and spells out the unique advantage of this method.

In minimising $L_r(\Phi^n, \mathbf{q}, \boldsymbol{\lambda}^n)$ with respect to \mathbf{q} in a discrete setting, we may locally minimize the integrand of $L_r(\Phi^n, \mathbf{q}, \boldsymbol{\lambda}^n)$ with respect to $\mathbf{q} \in X_e$, where X_e denotes the restriction of X to a particular discrete element, (e.g. a finite element), i.e. we find local values of \mathbf{p}^n from:

$$\mathbf{p}^n = \inf_{\mathbf{q}} \left\{ \frac{1}{2} \int_0^{|\nabla\Psi^* + \mathbf{q}|^2} \frac{\chi(s^{1/2})}{s^{1/2}} ds + \mathbf{q} \cdot \tilde{\mathbf{f}} + \frac{\tau_Y}{H} |\nabla\Psi^* + \mathbf{q}| + \frac{r}{2} |\mathbf{q}|^2 - (\boldsymbol{\lambda}^n + r\nabla\Phi^n) \cdot \mathbf{q} \right\} \quad (29)$$

Equivalently, we may find local values of \mathbf{p}^n from:

$$\mathbf{p}^n = \inf_{\mathbf{q}} \left\{ \frac{1}{2} \int_0^{|\nabla\Psi^* + \mathbf{q}|^2} \frac{\chi(s^{1/2})}{s^{1/2}} ds + \frac{\tau_Y}{H} |\nabla\Psi^* + \mathbf{q}| + \frac{r}{2} |\nabla\Psi^* + \mathbf{q}|^2 - (\boldsymbol{\lambda}^n + r(\nabla\Psi^* + \nabla\Phi^n) - \tilde{\mathbf{f}}) \cdot (\nabla\Psi^* + \mathbf{q}) \right\} \quad (30)$$

i.e. we have added terms independent of \mathbf{q} . This expression is minimized when $(\boldsymbol{\lambda}^n + r(\nabla\Psi^* + \nabla\Phi^n) - \tilde{\mathbf{f}})$ is parallel to $(\nabla\Psi^* + \mathbf{q})$. Thus, letting

$$\nabla\Psi^* + \mathbf{p}^n = \theta(\boldsymbol{\lambda}^n + r(\nabla\Psi^* + \nabla\Phi^n) - \tilde{\mathbf{f}}) \quad (31)$$

$$x = |\boldsymbol{\lambda}^n + r(\nabla\Psi^* + \nabla\Phi^n) - \tilde{\mathbf{f}}| \quad (32)$$

we have to find the minimizer of $M(\theta)$:

$$M(\theta) = \frac{1}{2} \int_0^{(\theta x)^2} \frac{\chi(s^{1/2})}{s^{1/2}} ds + \frac{\tau_Y}{H} |\theta|x + \frac{r}{2} (\theta x)^2 - \theta x. \quad (33)$$

Straightforwardly, if $x \leq \tau_Y/H$ then $\theta = 0$ minimizes $M(\theta)$, giving $\mathbf{p}^n = -\nabla\Psi^*$, (which corresponds to *unyielded* flow locally for that iteration). If $x > \tau_Y/H$ we find θ numerically from the one-dimensional equation

$$\chi(\theta x) + \frac{\tau_Y}{H} + r\theta x - x = 0. \quad (34)$$

which has a unique solution, (and here the flow is yielded on this iteration).

Informally at least, we can carry the physical interpretation further to see that if $\boldsymbol{\lambda}^n \rightarrow \boldsymbol{\mu}$, then the components of $\boldsymbol{\mu}$ give us a representation of the components of the pressure gradient, i.e.

$$\boldsymbol{\mu}_\phi = -\frac{\partial p}{\partial \xi}, \quad \boldsymbol{\mu}_\xi = \frac{\partial p}{\partial \phi}.$$

More correctly, since the pressure gradient (and \boldsymbol{S}) is indeterminate in those regions that are unyielded, $\boldsymbol{\mu}$ gives only an admissible pressure gradient, i.e. $\boldsymbol{\lambda}^n$ converges only to one particular choice for $\boldsymbol{S} + \tilde{\boldsymbol{f}}$.

3.1.2 Numerical implementation

Our implementation is relatively straightforward. We use a staggered rectangular mesh. The stream function variables, Ψ^* and Φ , are approximated at corner points and the fluid concentrations at the centre of each mesh control volume. The intermediate variables $\boldsymbol{\lambda}^n$ and \boldsymbol{q}^n are also approximated at the centre points. At each iteration of the algorithm we solve (28) for Φ_h^n using an SOR method with second-order accurate spatial fluxes. Due to the staggered mesh, this involves a 9 point stencil for Φ_h^n . Convergence is speeded by using the previously computed values Φ_h^{n-1} as an initial guess. The corner values of Φ_h^n are used to approximate $\nabla \Psi^*$ and $\nabla \Phi^n$ at the centre of each control volume and the locally one-dimensional problem for \boldsymbol{q}_h^n is solved, followed by the update for $\boldsymbol{\lambda}_h^n$.

We monitor convergence via the norm of $\boldsymbol{p}^{n+1} - \boldsymbol{p}^n$, on each timestep. This appears to be appropriate in the context of the whole problem, (i.e. solving (2) & (3) to simulate a displacement), since it is the velocity that is needed for solution of (2), rather than the streamfunction. The algorithm is found to converge satisfactorily, but not particularly quickly. At its heart we are solving an elliptic problem with a jump in material properties at the interface, and doing so on a fixed rectangular mesh. Unsurprisingly, convergence is quicker in situations where the interface aligns with the mesh. If the local convergence is tracked throughout the algorithm, we find slower convergence close to the interface and in unyielded regions. In terms of spatial accuracy, our discretisation seems to give $O(h)$ convergence. Obviously much of this could be improved through adaptive meshing and other discretisation techniques, but still the present algorithm produces results that compare well with our analytic solutions, as we will see in the following section.

For the solution of (2) at each time step we use the Flux Corrected Transport (FCT) scheme, which combines low-order (donor cell) and high-order (central difference) schemes, to minimize both numerical dispersion and diffusion during the advection. The FCT scheme preserves the jump in concentration at

the interface between fluids reasonably well, confining intermediate concentrations to a few mesh spacings. There are of course many alternative options for integrating (2) and we discuss some of these in §5. The FCT method has been implemented previously in a similar numerical computation, [18], and is found to be robust over a wide range of different simulation parameters.

4 Simulation of displacement dynamics

In simulating the entire wellbore, we come across the problems outlined in §1 of integrating over a large aspect ratio. Inevitably the accuracy will decrease with length and the computational time will increase, if one wishes to maintain a particular mesh size. Here we are more interested in determining that we have an accurate representation of the displacement dynamics and in investigating these dynamics. This can be done most effectively by considering the displacement in a frame of reference moving with the mean displacement speed, here unity. This is straightforward to do. The transformed coordinates are:

$$\phi = \bar{\phi}, \quad z = \xi - t. \quad (35)$$

The field equation for the stream function (3) is unchanged and for the concentration equation (2) we simply replace (\bar{v}, \bar{w}) with (v, w)

$$v = \bar{v}, \quad w = \bar{w} - 1. \quad (36)$$

We note that our numerical scheme is particularly well suited to this, since we have homogenised our stream function equation using

$$\Psi^* = \phi + \frac{e}{\pi} \sin \pi \phi, \quad (37)$$

which gives a velocity field of unit speed in the axial direction. Thus, the solution Φ of our homogenised problem is the stream function for the velocity field in the moving frame.

4.1 Steady state propagation in concentric annuli

To validate the accuracy of the algorithm we compare against an analytic representation of a steadily propagating interface. The existence of such steady state displacements was shown in [19] and the shape of the steady-state interface was derived analytically in the case of both concentric and mildly eccentric

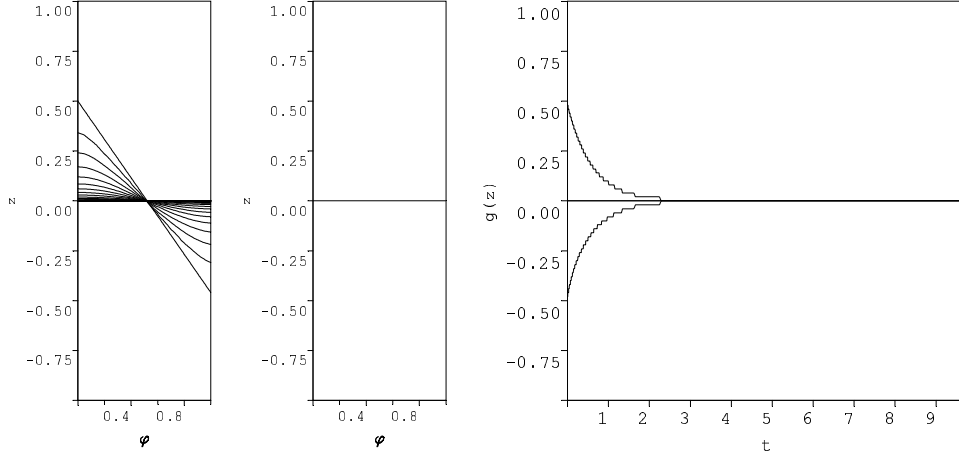


Fig. 3. Convergence of computational solution to stable steady state displacement: a) Successive contours of $g(\phi, t)$, (defined as $c(\phi, z, t) = 0.5$), at times $t = 0.0, 0.2, 0.4, \dots, 10.0$; b) Analytic steady state solution; c) Convergence of wide and narrow side interface positions, $g(0, t)$ & $g(1, t)$, to the steady state. Model parameters: $\beta = 0$, $e = 0$, $St = 0.1$, $\rho_1 = 1$, $\rho_2 = 0.9$, $\tau_{1,Y} = 0.9$, $\tau_{2,Y} = 0.7$, $\kappa_1 = 0.5$, $\kappa_2 = 0.4$, $m_1 = 1.0$, $m_2 = 1.2$.

annuli. In the moving frame we denote the interface position by $z = g(\phi, t)$. The steady state shape for a concentric annular displacement is

$$g(\phi) = -\frac{1}{\pi} \frac{b \sin \beta}{[\chi_k(1) + \tau_{k,Y}]_1^2 + b \cos \beta} \cos \pi \phi, \quad (38)$$

where b is the buoyancy parameter:

$$b = \frac{\rho_2 - \rho_1}{St^*}. \quad (39)$$

We present results of 3 simulations in Figs. 3-5. For all simulations we have fixed the fluid properties and process parameters at $e = 0$, $St = 0.1$, $\rho_1 = 1$, $\rho_2 = 0.9$, $\tau_{1,Y} = 0.9$, $\tau_{2,Y} = 0.7$, $\kappa_1 = 0.5$, $\kappa_2 = 0.4$, $m_1 = 1.0$, $m_2 = 1.2$. In the 3 simulations we vary the inclination of the annulus, from vertical (Fig. 3) to horizontal (Fig. 5). In each picture we show firstly a series of interface profiles, $z = g(\phi, t)$, which we define as the level set $c(\phi, z, t) = 0.5$. We integrate over a time interval $t \in [0, 10]$ and plot profiles at successive intervals $\Delta t = 0.2$. The mesh spacings are $\Delta \phi = 0.04$, $\Delta z = 0.02$.

For Fig. 3, where the steady state is perpendicular to the z -axis, we choose an oblique initial condition. For Figs. 4 & 5, we choose an initial condition perpendicular to the z -axis. In fact choice of initial condition proves not to be critically important. In each case it is seen that the interface profile converges rapidly to the steady state. Also shown in Figs. 3-5 are the analytic steady state profile (38), as well as a comparison of the wide and narrow side interface

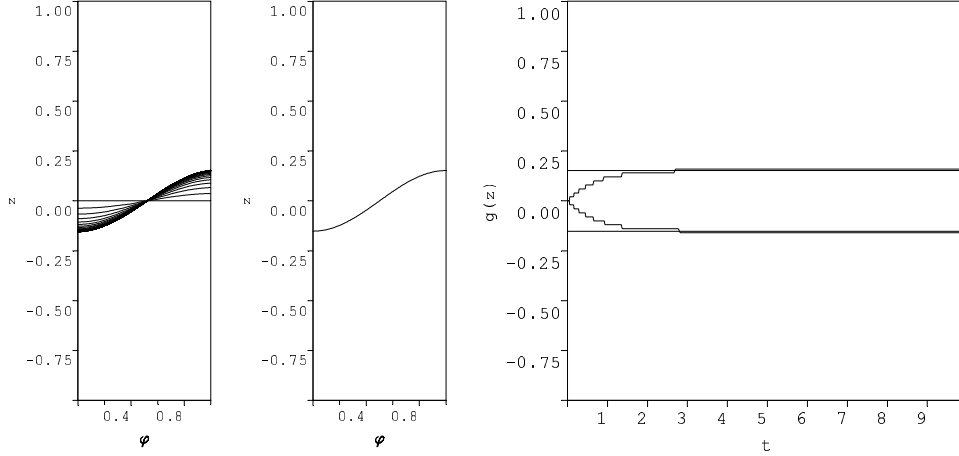


Fig. 4. Convergence of computational solution to stable steady state displacement: a) Successive contours of $g(\phi, t)$, (defined as $c(\phi, z, t) = 0.5$), at times $t = 0.0, 0.2, 0.4, \dots, 10.0$; b) Analytic steady state solution; c) Convergence of wide and narrow side interface positions, $g(0, t)$ & $g(1, t)$, to the steady state. Model parameters: $\beta = \pi/4$, $e = 0$, $St = 0.1$, $\rho_1 = 1$, $\rho_2 = 0.9$, $\tau_{1,Y} = 0.9$, $\tau_{2,Y} = 0.7$, $\kappa_1 = 0.5$, $\kappa_2 = 0.4$, $m_1 = 1.0$, $m_2 = 1.2$.

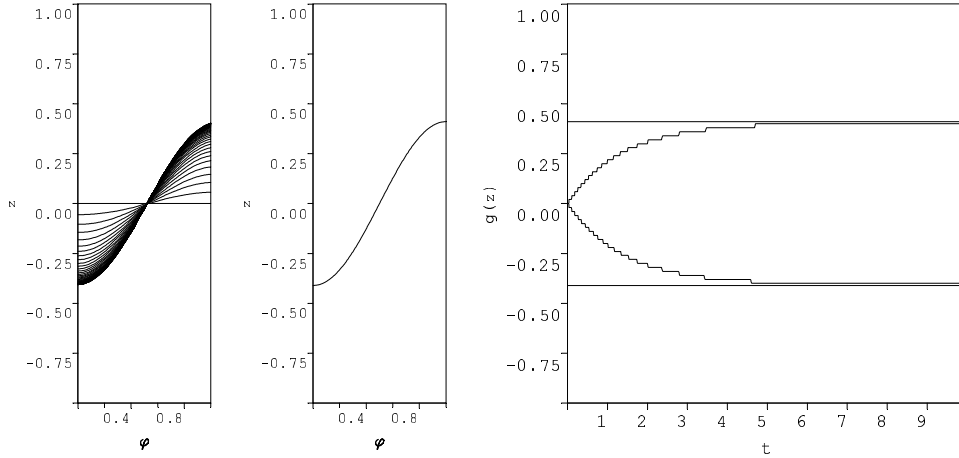


Fig. 5. Convergence of computational solution to stable steady state displacement: a) Successive contours of $g(\phi, t)$, (defined as $c(\phi, z, t) = 0.5$), at times $t = 0.0, 0.2, 0.4, \dots, 10.0$; b) Analytic steady state solution; c) Convergence of wide and narrow side interface positions, $g(0, t)$ & $g(1, t)$, to the steady state. Model parameters: $\beta = \pi/2$, $e = 0$, $St = 0.1$, $\rho_1 = 1$, $\rho_2 = 0.9$, $\tau_{1,Y} = 0.9$, $\tau_{2,Y} = 0.7$, $\kappa_1 = 0.5$, $\kappa_2 = 0.4$, $m_1 = 1.0$, $m_2 = 1.2$.

positions, $g(0, t)$ & $g(1, t)$, as they converge to $g(0)$ & $g(1)$. It can be observed that the numerical method produces a very good representation of the steady states, with accuracy of the order of a mesh point, which is anyway to be expected in evaluating $c(\phi, z, t) = 0.5$.

4.2 Stable steady states in mildly eccentric annuli

Also described in [19] is a perturbation method that yields the steady state shape when the annulus is mildly eccentric, $e \ll 1$, and when the concentric steady state profile is approximately perpendicular to the annulus axis. For eccentric annuli, the steady state will give a non-zero stream function solution u , since the far-field velocity field will not be uniform in ϕ . The steady state interface position from [19] is

$$g(\phi) \sim -\frac{1}{\pi} \frac{b \sin \beta}{[\chi_k + \tau_{k,Y}]_1^2 + b \cos \beta} \cos \pi \phi \quad (40)$$

$$-\frac{e}{\pi^2} \frac{\sum_{k=1,2} P(\chi_k, \tau_{k,Y}, m_k) (\chi_k + \tau_{k,Y}) \alpha_k \tanh \alpha_k L}{[\chi_k + \tau_{k,Y}]_1^2 + b \cos \beta} \cos \pi \phi,$$

where χ_k is evaluated at $(|\nabla\Psi|, H) = (1, 1)$, (i.e. we linearise about a concentric geometry). The positive parameters α_k are defined by

$$\alpha_k^2 = \frac{\pi^2 \chi'_k(1, 1)}{\chi_k(1, 1) + \tau_{k,Y}} > 0, \quad (41)$$

where $\chi'_k(1, 1)$ is the partial derivative of $\chi_k(|\nabla\Psi|, H)$ with respect to $|\nabla\Psi|$. The first term in (40) is seen to be exactly the concentric solution and the perturbation is of $O(e)$. In the derivation of (40) in [19], we have used the classical method of linearising not only about the zero-th order variables, but also about the zero-th order domain. The stream function $\Phi(\phi, z)$ is thus defined on the unperturbed domains and is given to $O(e^2)$ by:

$$\Phi(\phi, z) \sim eP(\chi_1(1, 1), \tau_{1,Y}, m_1) \left(1 - \frac{\cosh \alpha_1(L+z)}{\cosh \alpha_1 L}\right) \frac{\sin \pi \phi}{\pi}, \quad z < 0, \quad (42)$$

$$\Phi(\phi, z) \sim eP(\chi_2(1, 1), \tau_{2,Y}, m_2) \left(1 - \frac{\cosh \alpha_2(L-z)}{\cosh \alpha_2 L}\right) \frac{\sin \pi \phi}{\pi}, \quad z > 0, \quad (43)$$

where $P(\chi, \tau_Y, m)$ is the strictly positive function,

$$P(\chi, \tau_Y, m) = \frac{(m+1)^2 \chi^2 + (m+2)(2m+1) \chi \tau_Y + (m+1)(m+2) \tau_Y^2}{\chi[(m+1)\chi + (m+2)\tau_Y]}.$$

In order to compare our computational results with the eccentric perturbation solution, we take the parameters of our previous examples: $St = 0.1$, $\rho_1 = 1$,

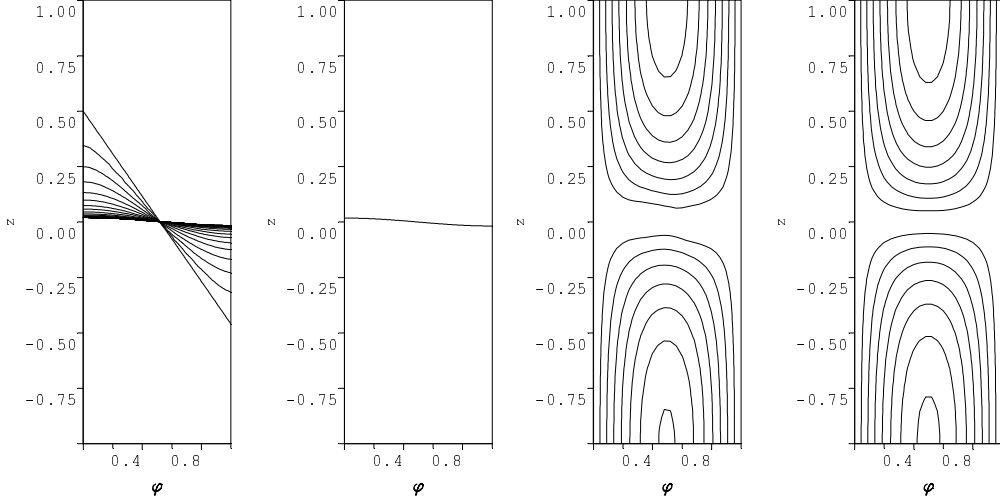


Fig. 6. Convergence of computational solution to stable steady state displacement at $e = 0.01$: a) Successive contours of $g(\phi, t)$, (defined as $c(\phi, z, t) = 0.5$), at times $t = 0.0, 0.2, 0.4, \dots, 10.0$; b) Perturbation steady state solution; c) Contours of the stream function solution computed at $t = 10$, (contour spacing 0.001); d) Perturbation solution for the stream function, (contour spacing 0.001). Model parameters: $\beta = 0$, $St = 0.1$, $\rho_1 = 1$, $\rho_2 = 0.9$, $\tau_{1,Y} = 0.9$, $\tau_{2,Y} = 0.7$, $\kappa_1 = 0.5$, $\kappa_2 = 0.4$, $m_1 = 1.0$, $m_2 = 1.2$.

$\rho_2 = 0.9$, $\tau_{1,Y} = 0.9$, $\tau_{2,Y} = 0.7$, $\kappa_1 = 0.5$, $\kappa_2 = 0.4$, $m_1 = 1.0$, $m_2 = 1.2$; fix $\beta = 0$ and increase the eccentricity from zero. Figs. 6-8 show the same simulation as in 3, but with eccentricities $e = 0.01, 0.05, 0.2$. As expected, for small e , convergence to the steady state shape is good. However, even for $e = 0.05$ there are noticeable differences between the analytical and computed stream functions. This is mainly due to the perturbation procedure used at the interface, i.e. the fluid domains are not equivalent. It might be thought that the solutions would converge in the far-field, but they do not. This is because the variation in far-field stream functions is not sinusoidal, whereas the analytic solutions show symmetry (and anti-symmetry for $g(\phi)$) about $\phi = 1/2$. As the eccentricity increases, symmetry about $\phi = 1/2$ is lost in the computational solution, see e.g. Fig. 8, although the solutions still converge to a stable steady state for sufficiently small e .

Remark 4.1 The stability of the steady state is not at all evident from the stream function contours shown in Figs. 6-8. The interface is the streamline $\Phi(\phi, z, t) = 0$, and the streamfunction contours are positive both above and below the interface. Thus, the velocity along the axis $\phi = 0$ is positive, both above and below the interface in the steady state case. Similarly, the velocity is negative above and below the steady state interface, on the axis $\phi = 1$. On the axis $\phi = 0$, the dynamics of the interface are simply governed by:

$$\frac{\partial g}{\partial t}(0, t) = w(0, g(0, t), t), \quad (44)$$

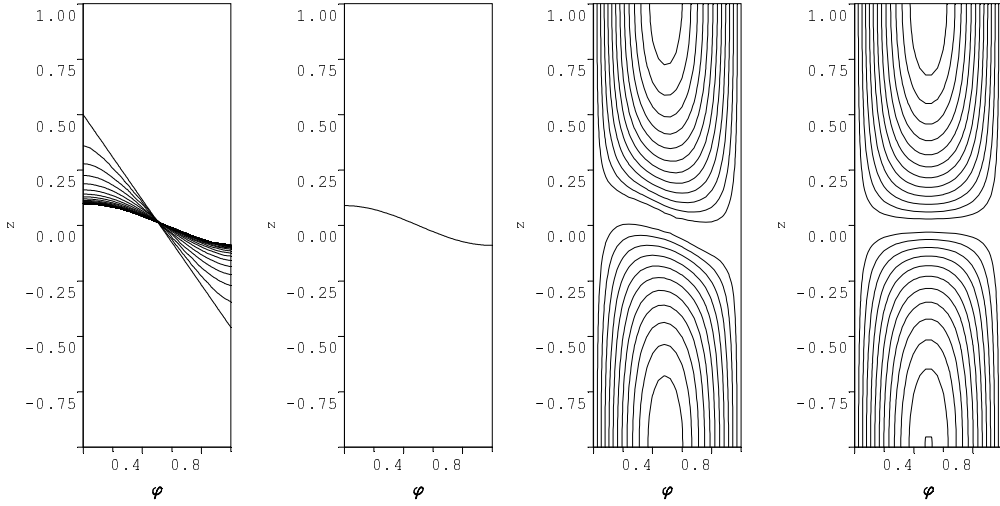


Fig. 7. Convergence of computational solution to stable steady state displacement at $e = 0.05$: a) Successive contours of $g(\phi, t)$, (defined as $c(\phi, z, t) = 0.5$), at times $t = 0.0, 0.2, 0.4, \dots, 10.0$; b) Perturbation steady state solution; c) Contours of the stream function solution computed at $t = 10$, (contour spacing 0.003); d) Perturbation solution for the stream function, (contour spacing 0.003). Model parameters: $\beta = 0$, $St = 0.1$, $\rho_1 = 1$, $\rho_2 = 0.9$, $\tau_{1,Y} = 0.9$, $\tau_{2,Y} = 0.7$, $\kappa_1 = 0.5$, $\kappa_2 = 0.4$, $m_1 = 1.0$, $m_2 = 1.2$.

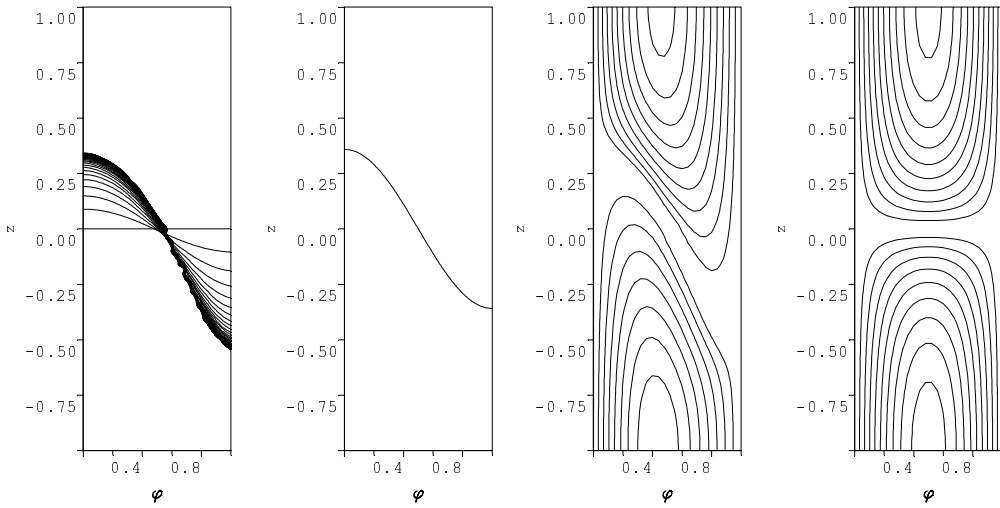


Fig. 8. Convergence of computational solution to stable steady state displacement at $e = 0.2$: a) Successive contours of $g(\phi, t)$, (defined as $c(\phi, z, t) = 0.5$), at times $t = 0.0, 0.2, 0.4, \dots, 10.0$; b) Perturbation steady state solution; c) Contours of the stream function solution computed at $t = 10$, (contour spacing 0.015); d) Perturbation solution for the stream function, (contour spacing 0.015). Model parameters: $\beta = 0$, $St = 0.1$, $\rho_1 = 1$, $\rho_2 = 0.9$, $\tau_{1,Y} = 0.9$, $\tau_{2,Y} = 0.7$, $\kappa_1 = 0.5$, $\kappa_2 = 0.4$, $m_1 = 1.0$, $m_2 = 1.2$.

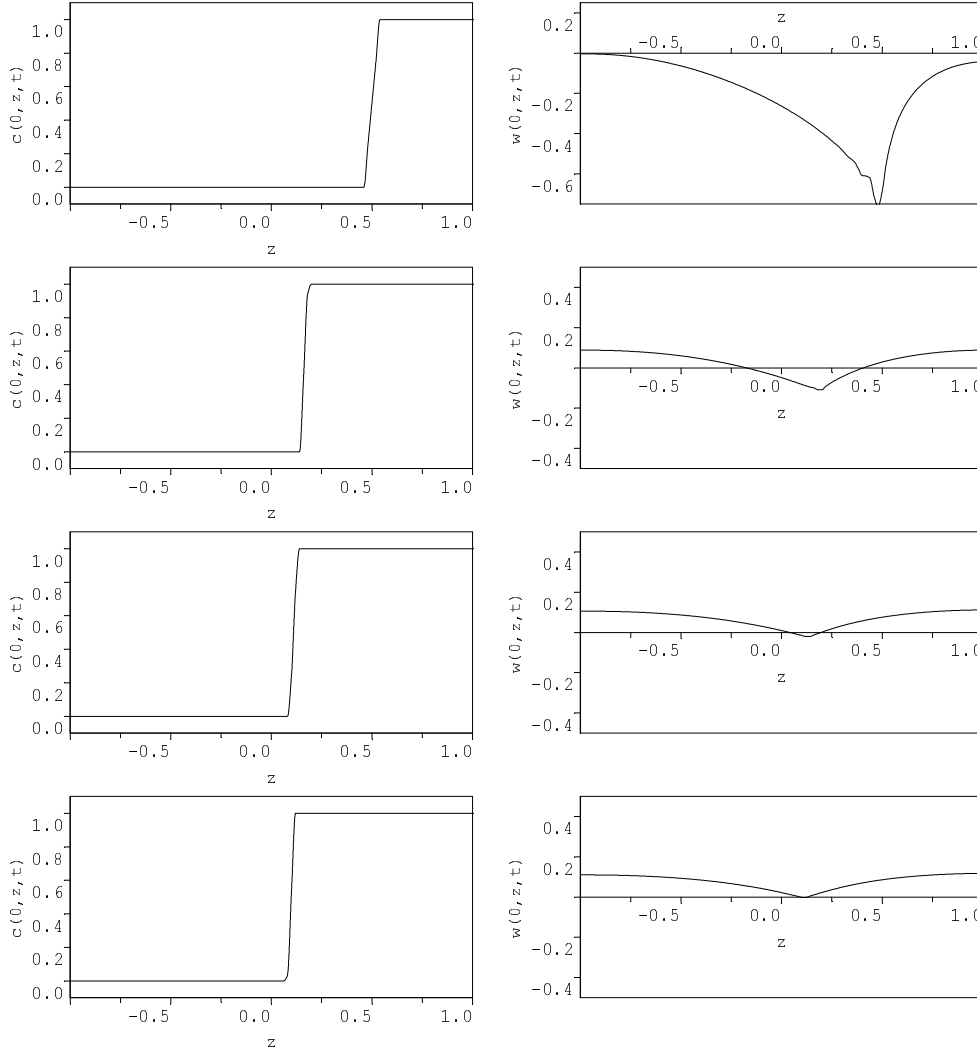


Fig. 9. Convergence of computational solution to stable steady state, along the axis $\phi = 0$, for an initial condition starting above the steady state interface. Left column shows the concentration $c(0, z, t)$ at successive times: $t = 0, 1, 2, 4$. Right column shows the axial velocity $w(0, z, t)$ at successive times: $t = 0, 1, 2, 4$. Model parameters: $e = 0.05$, $\beta = 0$, $St = 0.1$, $\rho_1 = 1$, $\rho_2 = 0.9$, $\tau_{1,Y} = 0.9$, $\tau_{2,Y} = 0.7$, $\kappa_1 = 0.5$, $\kappa_2 = 0.4$, $m_1 = 1.0$, $m_2 = 1.2$.

and similarly at $\phi = 1$. At first glance it therefore appears that the steady state is only metastable, i.e. stable from one side. However, this then begs the question of how a transient interface can ever evolve to the steady state. The error in this reasoning is that $\Phi(\phi, z, t) = \Phi(\phi, z; c)$, and the dependency on c is non-local. To illustrate this we examine numerically the convergence to the steady state of Fig. 7, (for $e = 0.05$), along the axis $\phi = 0$ for two different choices of initial condition. First, we take that in Fig. 7a, for which the initial interface lies above the steady state at $\phi = 0$. The results are shown in Fig. 9. Second we take an initially perpendicular interface, which lies below the steady state at $\phi = 0$. The results are shown in Fig. 10.

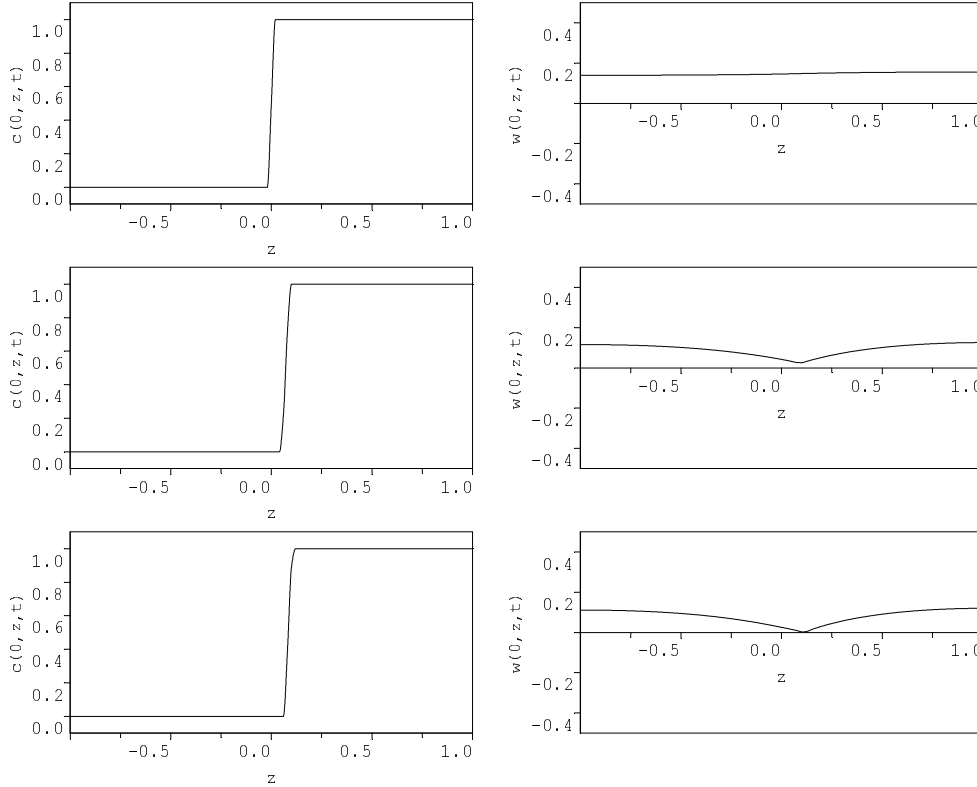


Fig. 10. Convergence of computational solution to stable steady state, along the axis $\phi = 0$, for an initial condition starting below the steady state interface. Left column shows the concentration $c(0, z, t)$ at successive times: $t = 0, 1, 2$. Right column shows the axial velocity $w(0, z, t)$ at successive times: $t = 0, 1, 2$. Model parameters: $e = 0.05$, $\beta = 0$, $St = 0.1$, $\rho_1 = 1$, $\rho_2 = 0.9$, $\tau_{1,Y} = 0.9$, $\tau_{2,Y} = 0.7$, $\kappa_1 = 0.5$, $\kappa_2 = 0.4$, $m_1 = 1.0$, $m_2 = 1.2$.

The results in Fig. 9 show that when the interface starts above the steady state, the velocity along the axis dips below zero over an interval in z which encompasses the interface position. The interface therefore drops downwards. As the interface approaches the steady state position, the interval of negative $w(0, z, t)$ decreases. Finally, in a fully converged situation, we have $w(0, z, t) > 0$, except at $z = g$. Conversely, if we examine the case when the interface starts below the steady state, Fig. 10, the velocity is initially strictly positive along $\phi = 0$, and the interface consequently rises. As the interface rises, $w(0, z, t)$ is suppressed ahead of the interface. This suppression increases as the steady state is approached and eventually we finish with $w(0, z, t)$ touching zero at exactly the steady state position. The situation is reversed on the narrow side.

In both cases, the converged steady state has a velocity profile $w(0, z)$ which one would classify as metastable, i.e. according to the one-dimensional model (44), but this is clearly not a correct classification of the interface dynamics, which appear to approach an asymptotically stable steady state. What is peculiar about this process of convergence and modification of the axial velocity is that the far-field velocities are always positive. The suppression of $w(0, z, t)$ close to the interface appears to be due to the fluid slowing down as

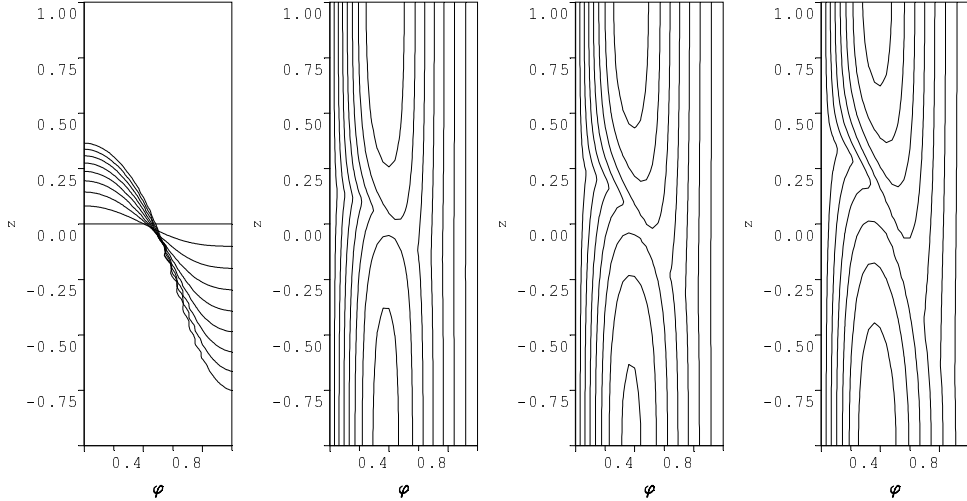


Fig. 11. Divergence of computational solution from an initially perpendicular interface with $e = 0.5$: (a) Successive contours of $g(\phi, t)$, (defined as $c(\phi, z, t) = 0.5$), at times $t = 0.0, 0.1, 0.2, \dots, 0.8$; (b)-(d) Contours of the stream function solution computed at $t = 0.2, 0.4, 0.8$, (contour spacing 0.04). Model parameters: $\beta = 0$, $St = 0.1$, $\rho_1 = 1$, $\rho_2 = 0.9$, $\tau_{1,Y} = 0.9$, $\tau_{2,Y} = 0.7$, $\kappa_1 = 0.5$, $\kappa_2 = 0.4$, $m_1 = 1.0$, $m_2 = 1.2$.

it is transferred from wide-side to narrow-side (below the interface) and from narrow-side to wide-side (above the interface).

4.3 Increasing eccentricity, loss of stability and mud channel formation

As the eccentricity is increased towards $e = 1$, at which point contact occurs on the narrow side, it is clear that a steady state simply cannot exist, i.e. since there is no-slip at the walls. For the example we have followed above, stability is lost at a value of $e < 0.3$. It is hard to evaluate computationally the critical value at which the stable steady state ceases to exist, (i.e. since the timescale for convergence becomes infinite at marginal stability), and an analytical method might be better suited. For larger eccentricities however, divergence of the interface is quite clear. As an example, in Fig. 11 we show the evolution of both the interface and streamlines at a number of successive timesteps, for $e = 0.5$, (all other parameters being as before). The interface clearly elongates from its initial position and there is no steady displacement.

Thus, the first qualitative change observed for increasing e is the loss of the steady state. The interface itself retains stability, in the sense that there is no evidence of secondary instabilities, e.g. viscous fingering. However, as the interface elongates our numerical method does lose accuracy and eventually has difficulty in coping with the changing orientation of the interface with respect to the mesh. At smaller values of e , the displacements first observed to be unsteady are flows that have fully mobile fluids all around the annulus.

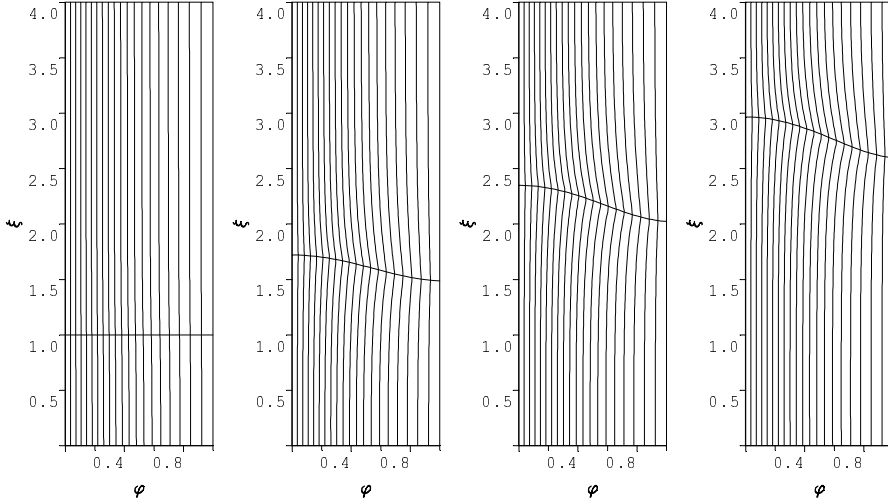


Fig. 12. Stable steady state interface propagation and streamlines in the fixed frame (ϕ, ξ) , with $e = 0.1$: times $t = 0.0, 0.6, 1.2, 1.8$. Streamlines at spacings $\Delta\Psi = 0.05$. Model parameters: $\beta = 0$, $St = 0.1$, $\rho_1 = 1$, $\rho_2 = 0.9$, $\tau_{1,Y} = 0.9$, $\tau_{2,Y} = 0.7$, $\kappa_1 = 0.5$, $\kappa_2 = 0.4$, $m_1 = 1.0$, $m_2 = 1.2$.

As the eccentricity increases further we can attain unsteady displacements that effectively *burrow* slowly up the narrow side. Here the far-field velocity fields are unyielded on the the narrow side of the annulus, but the interface still propagates! Although static in the far-field, in the vicinity of the interface the displacing fluid is forced over to the narrow side and the displaced fluid is forced away from the narrow side, ahead of the interface. Thus, a burrowing motion occurs. It is quite difficult to identify this regime, which appears to be a strictly intermediate state. The final qualitative transition occurs at higher still eccentricities, when the interface simply does not move on the narrow side of the annulus. In the cementing context, this corresponds to the formation of a static mud channel in the well, which is not removed by the cement.

The different regimes are easiest appreciated in the static frame of reference (ϕ, ξ) . In Figs. 12-15 respectively we show time-frames of the displacement for $e = 0.1$, (stable steady state), $e = 0.3$ (unsteady mobile), $e = 0.5$ (unsteady burrowing), $e = 0.8$ (static channel). For the stable steady state Fig. 12 the interface is still converging in the final frame shown. This underscores the utility of the moving frame computations, avoiding the necessity of long domains and large discretisation matrices. Qualitatively there is little different to observe between Figs. 13 & 14, but the velocity at the interface is significantly different. The burrowing interface barely moves on the narrow side. The fully static narrow-side channels are observable in Fig. 15 due to the static interface position.

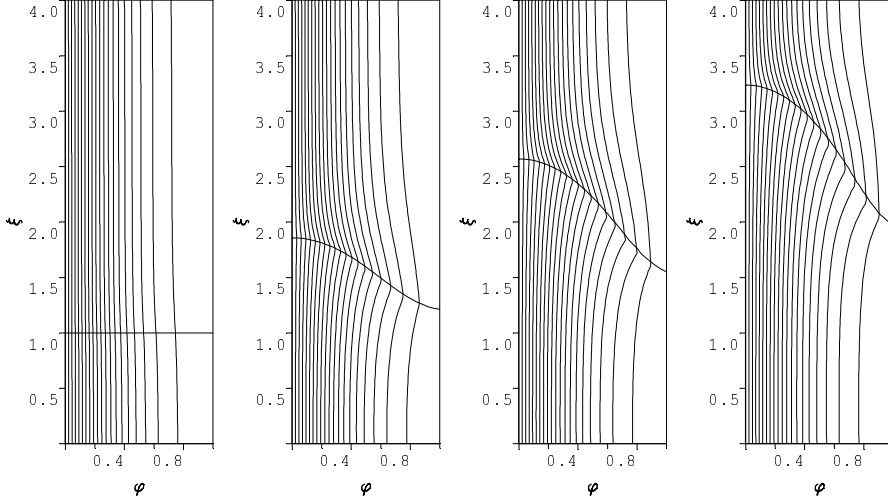


Fig. 13. Unstable but mobile interface propagation and streamlines in the fixed frame (ϕ, ξ) , with $e = 0.3$: times $t = 0.0, 0.6, 1.2, 1.8$. Streamlines at spacings $\Delta\Psi = 0.05$. Model parameters: $\beta = 0, St = 0.1, \rho_1 = 1, \rho_2 = 0.9, \tau_{1,Y} = 0.9, \tau_{2,Y} = 0.7, \kappa_1 = 0.5, \kappa_2 = 0.4, m_1 = 1.0, m_2 = 1.2$.

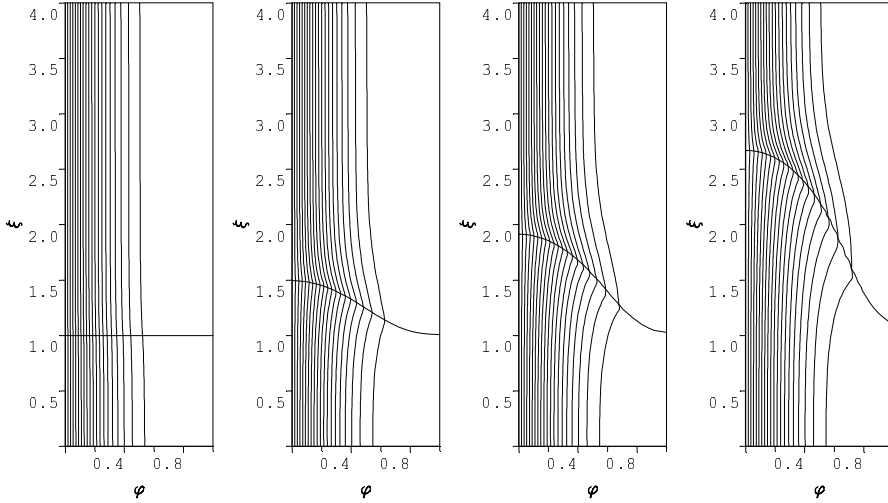


Fig. 14. Unstable but mobile interface propagation and streamlines in the fixed frame (ϕ, ξ) , with $e = 0.5$: times $t = 0.0, 0.3, 0.6, 1.2$. Streamlines at spacings $\Delta\Psi = 0.05$. Model parameters: $\beta = 0, St = 0.1, \rho_1 = 1, \rho_2 = 0.9, \tau_{1,Y} = 0.9, \tau_{2,Y} = 0.7, \kappa_1 = 0.5, \kappa_2 = 0.4, m_1 = 1.0, m_2 = 1.2$.

5 Discussion and conclusion

In this paper we have described the application of an iterative augmented Lagrangian algorithm to solution of a model describing the annular displacement of non-Newtonian fluids. Coupled with numerical solution of the concentration equation, this algorithm has allowed us to produce numerical simulations of two-dimensional primary cementing displacement flows. We have demonstrated that our algorithm is able to accurately reproduce analytical test case

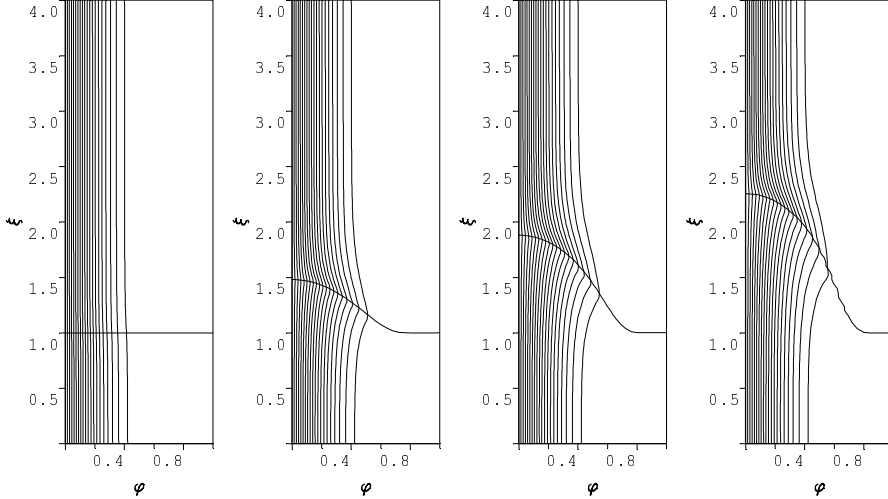


Fig. 15. Static mud channel formation, interface propagation and streamlines in the fixed frame (ϕ, ξ) , with $e = 0.8$: times $t = 0.0, 0.3, 0.6, 0.9$. Streamlines at spacings $\Delta\Psi = 0.05$. Model parameters: $\beta = 0$, $St = 0.1$, $\rho_1 = 1$, $\rho_2 = 0.9$, $\tau_{1,Y} = 0.9$, $\tau_{2,Y} = 0.7$, $\kappa_1 = 0.5$, $\kappa_2 = 0.4$, $m_1 = 1.0$, $m_2 = 1.2$.

solutions, i.e. for the concentric annulus.

Although we have studied a simplified version of the model in [18], the algorithm we have used is equally applicable to slowly varying annular geometries. The augmented Lagrangian method converges stably for all physically sensible fluid properties. However, although the criterion for convergence (27) is independent of fluid properties, there are certainly differing speeds of convergence for different fluid properties, different concentration fields (interfaces) and different geometries.

In considering extending application of this algorithm to displacements taking place over the scale of the wellbore, the main restriction comes in computational speed, whilst maintaining accuracy. Using the augmented Lagrangian method for the solution of (3) will generally be slower than using a regularisation method, e.g. replacing (6) & (7) with

$$\mathbf{S} = \left[\frac{\chi(|\nabla\Psi|) + \tau_Y/H}{(|\nabla\Psi|^2 + \epsilon^2)^{1/2}} \right] \nabla\Psi, \quad \epsilon \ll 1, \quad (45)$$

and solving (3). However, the key question is whether one wishes to determine unyielded zones or not. Although one can use a regularisation such as (45) and one can prove convergence of the solutions to that of the *exact* model as $\epsilon \rightarrow 0$, there is no proof of convergence of the pressure gradient fields. In practice one must use a small finite ϵ for computation and two problems arise. First, one must interpret which domains are in fact unyielded, e.g. by comparing $|S|$ with τ_Y/H , but this must be justified. Secondly, there will be a error of order $\delta(\epsilon)$, (to be determined), between the regularised and exact stream functions. As

the simulation progresses this error can accumulate over the timescale of the simulation $t \sim Z \gg 1$. Thus, we can expect a cumulative error of size $Z\delta(\epsilon)$ over the length of a simulation, which is potentially significant. This error will affect the final placement of fluids and, since using (45) allows fluids to move, the regularised method will give an overly optimistic prediction of the effectiveness of mud removal. Note that this is simply due to the transient nature of the problem and the long timescales involved in cementing displacements. For a static computation, usage of a regularisation such as (45) is much less problematic.

Even allowing for the above problems, the regularisation method leads to a two-dimensional nonlinear Poisson equation. Although fast and robust solvers can be devised, the overall computation time for the simulation of a real cementing job may still be too long to be used repeatedly for job design in a field setting. Thus, pseudo-two-dimensional methods such as the perturbation method in [18] retain some advantages for practical application.

A completely different application of this type of algorithm, with minor modifications, would be to study and simulate non-Darcy flows of non-Newtonian fluids through porous media. In particular, the flows of certain heavy oils in porous media exhibit similar flow characteristics, in that they have a limiting pressure gradient which must be overcome before they flow, see e.g. [30,31]. In fact the first ideas of modelling cementing displacements in this way, (see [20]), were derived from a porous media flow analogy. Obviously in a reservoir setting, timescales are even longer than here and the ability to predict static regions of oil is very valuable.

The second restriction in our computational algorithm has been in the use of the FCT method and adoption of a regular rectangular mesh. The limitations are most evident when the interface tends to elongate, resulting in a loss of accuracy. The FCT method itself performs well and has good conservation properties, (e.g. observe in Figs. 9 & 10 that the displacement front at $\phi = 0$ remains well defined), but the regular mesh is not well suited to this problem. We are investigating use of adaptive meshing and level set techniques.

Regarding the implications of our results. We have shown very clearly the dominating effect of eccentricity in determining qualitatively how effective the displacement is likely to be. In general for stable interfaces, (see discussion below), as the eccentricity increases we pass through 3 qualitative states:

- (1) Stable steady state interfaces, (a travelling wave solution);
- (2) Stable but unsteady mobile interfaces, (including both fully mobile fluids and burrowing motions);
- (3) Stable unsteady interfaces that are immobile on the narrow side of the annulus, (mud channel formation).

Whilst, it is clear that the last case is the worst case, since mud will remain in the well, the unsteady interfaces are also bad news. Typically cementing volumes are judged to fill the intended annular spaces and there is no continual pumping. Thus, the slower motion of the narrow side interface is also likely to mean a mud channel will form on the narrow side, since the mud will not be fully removed at the end of the cementing job. Whether this is detected operationally will depend on the type of job, e.g. in cementing a full-length casing, presumably one would see cement returns at surface and deduce that the narrow side mud was not being removed fast enough, but in a liner job this might not be observed at all. Thus, one must really view the transition between the above states as being a continual progression from a *good* to *bad* displacement.

We emphasize that in our simulations, we have seen no evidence of local instability of the interface for these fluid properties. It is physically intuitive, (and also industrial practice wherever possible), that one uses a more viscous and denser displacing fluid than displaced fluid, (unless of course the well is near to horizontal, where density effects are not necessarily helpful). This is the type of displacement that we have studied in this paper. We believe that there will be a significant parameter regime in which such (intuitively) stable displacements fronts are found, (i.e. broadly speaking: positive density and rheological differences between displacing and displaced fluids, non-horizontal annuli). For such parameters, it is felt that similar patterns of transition from stable steady state to unsteady interface to mud channel will occur, and our conclusions above are general in this sense.

If we move outside of the realm of intuitively stable displacements, it is possible to find a wide range of unstable situations. In particular, if we simply reverse the rheological parameters and densities between displaced and displacing fluids, a stable interface typically becomes unstable. We show just one example of this below, in Fig. 16, where we have reversed the fluid properties above, for the case $e = 0.01$. The initially perpendicular interface becomes rapidly unstable. We note that the analytical prediction of a steady state displacement profile is still valid for these parameters, (and is identical with that shown in Fig. 6b). It is simply that the steady state is unstable. This type of instability is believed to be of the type observed in viscous fingering studies. Our computational method is unsuitable for the study of this type of unstable displacement. It is clearly of value to predict the onset of this type of instability, since it represents a limitation of our model. For this, analytical methods are probably more appropriate than computational. Some progress has been made on this type of problem for yield stress fluids, see e.g. [32–37].

A second potential cause of instabilities is when the physical assumptions underlying the model itself begin to break down. For example, the assumption of homogeneity of fluid across the annular gap, which is commonly made in

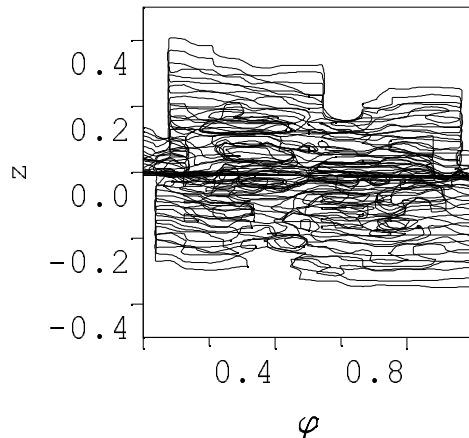


Fig. 16. Successive contours of $g(\phi, t)$, (defined as $c(\phi, z, t) = 0.5$), at times $t = 0.0, 0.05, 0.1, \dots, 1.0$, for an unstable and unsteady displacement. Model parameters: $e = 0.01$, $\beta = 0$, $St = 0.1$, $\rho_1 = 0.9$, $\rho_2 = 1$, $\tau_{1,Y} = 0.7$, $\tau_{2,Y} = 0.9$, $\kappa_1 = 0.4$, $\kappa_2 = 0.5$, $m_1 = 1.2$, $m_2 = 1.0$.

Hele-Shaw displacements, will become questionable at very long times due to Taylor dispersion and molecular diffusion, as discussed in [18]. A further area that needs study, is the effect of the cross-flow that is evident at the interface in the streamline plots in the moving frame. Whilst in our examples this effect is weaker than the mean flow, there may be other situations where the effect is significant and gives rise to Kelvin-Helmholtz like instabilities. There is some evidence for interfacial shear instabilities on the narrow-side reported in the experiments of [21,22], although the authors there also discuss buoyancy effects as a possible cause. Of course, in the Hele-Shaw modelling approach only the normal stress and normal component of velocity are continuous at the interface. Thus, our model effectively serves as the outer solution for an interfacial boundary layer flow which would need to be studied. For miscible fluids, it is likely that both above effects result in local mixing of some description, close to the interface. Studies of interest include addressing whether or not such a mixing zone reaches an equilibrium limiting thickness and secondly, what is the effect of fluid incompatibility on mixture models such as we have used here.

Acknowledgements:

This research has been carried out at the University of British Columbia, supported financially by Schlumberger and NSERC through CRD project 245434, as well as by the Pacific Institute for the Mathematical Sciences. This support is gratefully acknowledged.

References

- [1] E.B. Nelson. *Well Cementing*. Schlumberger Educational Services, (1990).
- [2] C.W. Sauer. *Mud displacement during cementing: A state of the art*. Journal of Petroleum Technology, pages 1091-1101, September (1987).
- [3] Primary and Remedial Cementing Guidelines. Drilling and Completions Committee, Alberta, April 1995. Distributed by the Petroleum Industry Training Service.
- [4] M.J. Economides, Implications of Cementing on Well Performance. In: E. B. Nelson (ed.), *Well Cementing*. Schlumberger Educational Services, (1990) chapter 1.
- [5] K. Newman, Cement pulsation improves gas well cementing. *World Oil*, July 2001, 89-94.
- [6] B. Nichol, Choosing Economic Options for Shut-in Wells with a Risk Assessment Approach. Presentation at: *Cost-effective Abandonment Solutions, Technology Information Session*, Calgary May 3, 2000. Meeting organised by PTAC (Petroleum Technology Alliance Canada).
- [7] D. Dustrehoft, G. Wilson and K. Newman, Field Study on the Use of Cement Pulsation to Control Gas Migration. *Society of Petroleum Engineers* paper number SPE 75689 (2002).
- [8] R.H. McLean, C.W. Manry and W.W. Whitaker, Displacement Mechanics in Primary Cementing. *Society of Petroleum Engineers* paper number SPE 1488 (1966).
- [9] A. Jamot. *Displacement de la boue par le latier de ciment dans l'espace annulaire tubage-paroi d'un puits*. Revue Assoc. Franc. Techn. Petr., 224, pp.27-37, (1974).
- [10] C.F. Lockyear and A.P. Hibbert. *Integrated Primary Cementing Study Defines Key Factors for Field Success*. Journal of Petroleum Technology, December (1989).
- [11] C.F. Lockyear, D.F. Ryan and D.F. Gunningham. *Cement Channeling: How to Predict and Prevent*. Society of Petroleum Engineers, Paper number SPE 19865, (1989).
- [12] M. Couturier, D. Guillot, H. Hendriks and F. Callet. *Design Rules and Associated Spacer Properties for Optimal Mud Removal in Eccentric Annuli*. Society of Petroleum Engineers, Paper number SPE 21594, (1990).
- [13] S. Brady, P.P. Drecq, K.C. Baker, D.J. Guillot. *Recent Technological Advances Help Solve Cement Placement Problems in Gulf of Mexico*. Society of Petroleum Engineers, Paper number IADC SPE 23927, (1992).

- [14] V.C. Kellessidis, R. Rafferty, A. Merlo, R. Maglione. *Simulator Models U-tubing to improve primary cementing*. Oil and Gas Journal, March (1994).
- [15] N.A. Barton, G.L. Archer and G.L. Seymour. *Computational fluid dynamics improves liner cementing operation*. Oil and Gas Journal, September (1994).
- [16] E.H. Vefring, K.S. Bjorkevoll, S.A. Hansen, N. Sterri, O. Saevareid, O. Aas and O. Merlo. *Optimization of Displacement Efficiency During Primary Cementing*. Society of Petroleum Engineers, Paper number SPE 39009, (1997).
- [17] P. Szabo and O. Hassager. *Displacement of one Newtonian fluid by another: density effects in axial annular flow*. Int. J. Multiphase Flow **23**(1), pp. 113-129, (1997).
- [18] S.H. Bittleston, J. Ferguson and I. Frigaard. *Mud removal and cement placement during primary cementing of an oil well; laminar non-Newtonian displacements in an eccentric Hele-Shaw cell*. J. Engng. Math., **43**, pp. 229-253 (2002).
- [19] S. Pelipenko and I.A. Frigaard. *On steady state displacements in primary cementing of an oil well*. Submitted to J. Engng. Math., August (2002).
- [20] M. Martin, M. Latil and P. Vetter. *Mud Displacement by Slurry During Primary Cementing Jobs - Predicting Optimum Conditions*. Society of Petroleum Engineers, Paper number SPE 7590, (1978).
- [21] A. Tehrani, J. Ferguson and S.H. Bittleston, Laminar Displacement in Annuli: A Combined Experimental and Theoretical Study. *Society of Petroleum Engineers* paper number SPE 24569 (1992).
- [22] A. Tehrani, S.H. Bittleston and P.J.G. Long, Flow instabilities during annular displacement of one non-Newtonian fluid by another. *Experiments in Fluids* 14 (1993) 246-256.
- [23] M. Allouche, I.A. Frigaard and G. Sona. *Static wall layers in the displacement of two visco-plastic fluids in a plane channel*. J. Fluid Mech., 424, pp. 243-277 (2000).
- [24] I.A. Frigaard, O. Scherzer and G. Sona. *Uniqueness and non-uniqueness in the steady displacement of two visco-plastic fluids*. ZAMM, 81(2), pp. 99-118 (2001).
- [25] I.A. Frigaard, M. Allouche and C. Gabard. *Incomplete displacement of viscoplastic fluids in slots and pipes; implications for zonal isolation*. Society of Petroleum Engineers paper number: SPE 64998, February (2001).
- [26] I.A. Frigaard, S. Leimgruber and O. Scherzer. *Variational methods and maximal residual wall layers*. Submitted to J. Fluid Mechanics, March (2002).
- [27] M. Fortin and R. Glowinski. *Augmented Lagrangian Methods*. North-Hollan, (1983).
- [28] R. Glowinski. *Numerical Methods for Nonlinear Variational Problems*. Springer-Verlag, (1983).

- [29] R.R. Huilgol and M.P. Panizza. *On determination of the plug flow region in Bingham fluids through the application of variational inequalities*. *J. Non-Newtonian Fluid Mech.*, 58, 1995.
- [30] G.I. Barenblatt, V.M. Entov, and V.M. Ryzhik, Theory of fluid flows through natural rocks. *Theory and Applications of Transport in Porous Media* volume 3 Kluwer (1990) pp. 44-51, 197-222.
- [31] R.V. Goldstein and V.M. Entov. *Qualitative Methods in Continuum Mechanics* (1989) 279pp.
- [32] H. Pascal, Rheological behaviour effect of non-Newtonian fluids on dynamic of moving interface in porous media. *Int. J. Engng. Sci.* 22(3) (1984) 227-241.
- [33] H. Pascal, Dynamics of moving interface in porous media for power law fluids with a yield stress. *Int. J. Engng. Sci.* 22(5) (1984) 577-590.
- [34] H. Pascal, A theoretical analysis of stability of a moving interface in a porous medium for Bingham displacing fluids and its application in oil displacement mechanism. *Can. J. Chem. Engng.* 64 (1986) 375-379.
- [35] S.D.R. Wilson, The Taylor-Saffman problem for a non-Newtonian liquid. *J. Fluid Mech.* 220 (1990) 413-425.
- [36] V.A. Gorodtsov and V.M. Yentov, Instability of the displacement fronts of non-Newtonian fluids in a Hele-Shaw cell. *J. Appl. Maths Mechs.* 61 (1997) 111-126.
- [37] P. Coussot, Saffman-Taylor instability in yield-stress fluids. *J. Fluid Mech.* 380 (1999) 363-376.